ACS OMEGA

Article

http://pubs.acs.org/journal/acsodf

Realization of Fractal-Inspired Thermoresponsive Quasi-3D Plasmonic Metasurfaces with EOT-Like Transmission for Volumetric and Multispectral Detection in the Mid-IR Region

Dihan Hasan,[†,‡,§] Chong Pei Ho,[†,‡,§] and Chengkuo Lee*[,†,‡,§,⊥]

[†]Department of Electrical & Computer Engineering and [‡]Center for Intelligent Sensors and MEMS, National University of Singapore, 4 Engineering Drive 3, Singapore 117576

[§]NUS Suzhou Research Institute (NUSRI), Suzhou Industrial Park, Suzhou 215123, P. R. China

[⊥]Graduate School for Integrative Science and Engineering, National University of Singapore, 4 Engineering Drive 3, Singapore 117576

Supporting Information

ABSTRACT: We use a paradigmatic mathematic model known as *Sierpiński* fractal to reverse-engineer artificial nanostructures that can potentially serve as plasmonic metasurfaces as well as nanogap electrodes. Herein, we particularly demonstrate the possibility of obtaining multispectral extraordinary optical transmission-like transmission peaks from fractal-inspired geometries, which can preserve distinct spatial characteristics. To achieve enhanced volumetric interaction and thermal responsiveness within the framework, we consider a bilayer, quasi-three-dimensional (3D) configuration that relies on the unique approach of combining complementary and noncomplementary surfaces, while avoiding the need for multilayer alignment on the nanoscale. We implement an improved version of the model to (1) increase the volume of quasi-3D nanochannels and enhance the lightening-rod effect of the metasurfaces, (2) harness cross-coupling as a mechanism for achieving better sensitivity, and (3) exploit optical magnetism for pushing the resonances to longer wavelengths on a miniaturized platform. We further demonstrate vertical coupling as an effective route for ultimate miniaturization of such quasi-3D nanostructures. We report a wavelength shift up to 1666 nm/refractive index unit and 2.5 nm/°C, implying the usefulness of the proposed devices for applications such as dielectrophoretic sensing and nanothermodynamic study of molecular reactions in the chemically active mid-IR spectrum.

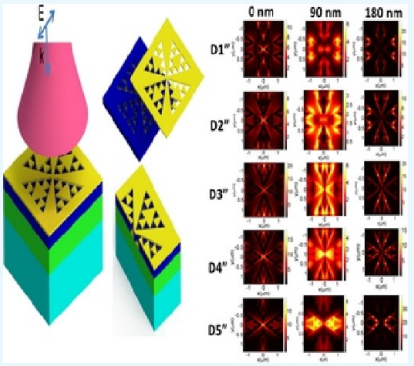

INTRODUCTION

In the last few years, the field of plasmonics has received extensive attention from researchers because of plasmon's formidable ability to couple free-space electromagnetic excitation into a nanoscale volume and enhance near-field optical intensity. Such a unique advantage of metal optics paves the way for engineering light−matter interactions more feasibly, and with the recent advancement in nanotechnology, plasmonics has become the burgeoning research topic in energy harvesting, telecom, and sensing industries.[1−5] High-refractive-index dielectrics are also becoming a focus of interest in light-harvesting applications due to their notable capability of enhancing near- and far-field light−matter interactions.[6−9] The virtue of this emerging platform lies in its low optical loss and potential compatibility with the silicon-based CMOS process. Nevertheless, the performance of conventional 2D plasmonic devices in sensing applications is still strongly limited by the rapid decay of the electric field as the distance from the metal surface increases. This bottleneck of distance-limited 2D devices can be addressed by extending the dimension of the field interaction as that in three-dimensional (3D) or quasi-3D configurations and therefore achieving volumetric field enhancement, providing a higher degree of access to the surrounding material and a larger surface area.[10,11] Furthermore, the 3D nature of the device can generate complex transmission spectra, which are quite likely to be more sensitive to the structural perturbation.[12] Besides, the bilayer quasi-3D structures with increased interaction volume can potentially achieve high sensitivity to external stimulation, for instance, temperature, as opposed to the conventional single-layer thermoplasmonic sensor.[13] Therefore, the quasi-3D configuration only requiring single-step lithography can be considered as a feasible solution toward improving the performance of the existing plasmonic sensors. However, the quasi-3D structures reported to date are mainly based on a simple nanohole or nanodisk structure and targeted for limited applications in the visible and near-IR ranges.[14−17] More complicated nanostructures are yet to be explored to achieve new functionalities at the expense of a higher fabrication tolerance. Among the various categories of nanostructures reported so far to manipulate

Received: August 21, 2016
Accepted: September 28, 2016
Published: November 4, 2016

DOI: 10.1021/acsomega.6b00201
ACS Omega 2016, 1, 818−831

localized surface plasmon resonance, the bow-tie architecture holds a unique position because of its extremely large field enhancement, partially aided by the lightening-rod effect at the sharp tips. It has been used as the key element for many high-performance plasmonic applications, such as nanolithography[18] ultra-low-power optical trapping,[19] single-molecule fluorescence detection,[20] extreme UV generation,[21] and as a plasmonic photography film for high-density storage.[22] On the other hand, fractal plasmonics is currently receiving the attention of researchers to engineer broadband characteristics of optical devices on a nanoscale because of the self-similarity and precisely defined mathematical model of fractal. Fractal nanostructures have already been exploited for subdiffraction focusing,[23] transparent metallic electrodes,[24] photovoltaic efficiency enhancement,[25] molecular fluorescence and surface-enhanced Raman spectroscopy enhancement,[26,27] broadband light trapping,[28] and, lately, multimodal broadband resonances with degeneracies.[29] Fortunately, the well-known *Sierpiński* fractal model is perfectly compatible with the state-of-the-art bow-tie nanostructure, and in this work, we particularly attempt to merge the two resourceful design platforms to achieve several specific research goals. First, we exploit the scalable resonance paths of the fractal layouts to obtain extraordinary optical transmission (EOT)-like multispectral peaks, which have a broad range of applications in interferometric sensing[30] and self-calibrated surface-enhanced infrared absorption spectroscopy (SEIRA).[31] Second, we consider the corners of the fractal geometries as reverse-engineered routes for scaling up the number of electric field "hotspots" in applications such as dielectrophoretic cell trapping.[32,33] Here, we implement an upgraded version of the fractal layouts not only to avoid the long-standing singularity issue of fractals but also to achieve enhanced electromagnetic properties, such as volumetric light–matter interactions, optical magnetism,[34−36] and cross-coupling.[37,38] We believe that the demonstration can be extended further for judiciously designed dielectric metasurfaces to realize low-loss sensing, light guiding, and spectroscopic applications.[6−9] The overall organization of our work will be as follows: a systematic conceptualization of the fractal-inspired metasurfaces; proof-of-concept demonstration of the EOT-like peaks for volumetric sensing; demonstration of vertical coupling of the quasi-3D structures for ultimate miniaturization; and, finally, demonstration of volumetric refractive sensing and enhanced thermoresponsive characteristics of the proposed platform.

DESIGN METHODOLOGY

Arrangement of the Fractalized Complementary and Noncomplementary Layouts. In Figure 1a–c, we show the evolution of Sierpiński fractal surfaces of orders 1 and 2 from the host equilateral triangle. A pattern of a given order is generated by subdividing the remaining triangles into four smaller congruent triangles, while removing the center one. Note that the solid triangular components of an ideal fractal antenna touch each other at a single point, which is why collective excitation of all of the components cannot be possible, due to the geometric singularity. Achieving such singularity by the state-of-the-art patterning techniques is also not feasible. Figure 1 depicts the chronological development of the modified abstraction considered in this work. In Figure 1k,l, we show the polarization-independent cross-coupled configurations of two different orders (M1 and M2) of fractalized devices on an oxide-coated substrate. Here, the modified fractal

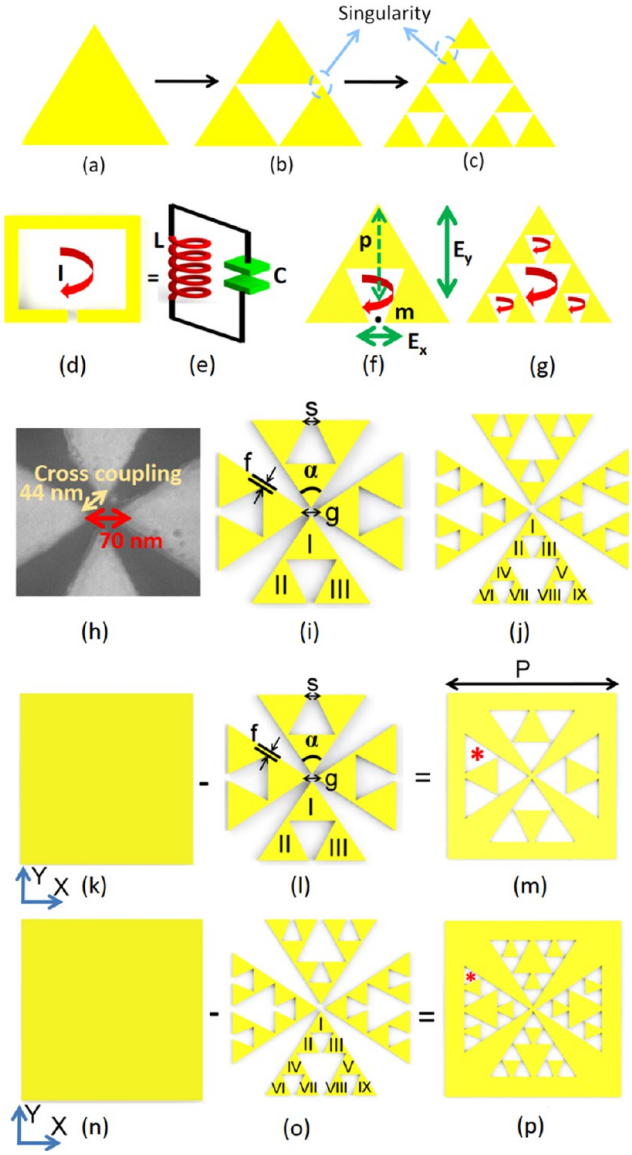

Figure 1. (a) Triangle without any fractal inclusion and *Sierpiński* fractal layout of (b) order 1 and (c) order 2. The presence of geometric singularity at the acute corners is indicated. (d) Conventional split ring with circulating current (I), and its (e) equivalent LC circuit model and (f) modified *Sierpiński* triangle of order 1, with a narrow conduction path at the previously indicated singularity zones and a split gap for magnetic excitation. **P** and **m** denote the moments of the dipolar mode and magnetic mode, respectively. (g) Modified *Sierpiński* triangle of order 2, with a scaled-up number of magnetic pathways. (h) Cross-coupling between the vertical and horizontal bow-tie pairs located at a proximity of nanoscale to each other. Cross-coupled configuration derived from the (i) first-order fractal layout and (j) second-order fractal layout. f and s denote the widths of the conduction path and split gap, respectively, whereas the roman numbers indicate the self-symmetric radiators of the fractal patterns. (k–m) Formation of the first-order complementary pattern. (n–p) Formation of the second-order complementary pattern. The red star indicates the nanosized aperture obtained through such a transformation. Pitch P is reduced to 2.77 μm to miniaturize the overall footprint and maximize the near-field coupling. The height of each fractal triangle has been kept fixed at 2.55 μm throughout the work.

triangle constitutes one of the four arms of the cross-coupled patterns. We provide the parameter offset (f) not only to avoid the geometric singularities in the simulation and fabrication but

DOI: 10.1021/acsomega.6b00201
ACS Omega 2016, 1, 818–831

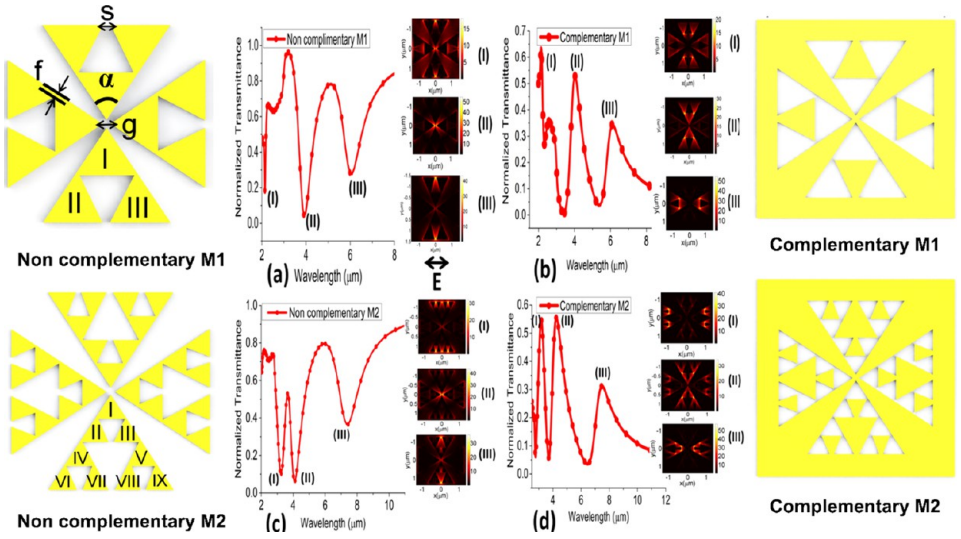

Figure 2. Normalized transmittance of (a) noncomplementary M1, (b) complementary M1, (c) noncomplementary M2, and (d) complementary M2 along with the corresponding resonant electric field distributions. The parameters *f* and *s* are fixed at 70 and 100 nm, respectively. The resonances are marked by (I), (II), and (III) in the spectra. Polarization of the incident light is shown by a double arrow.

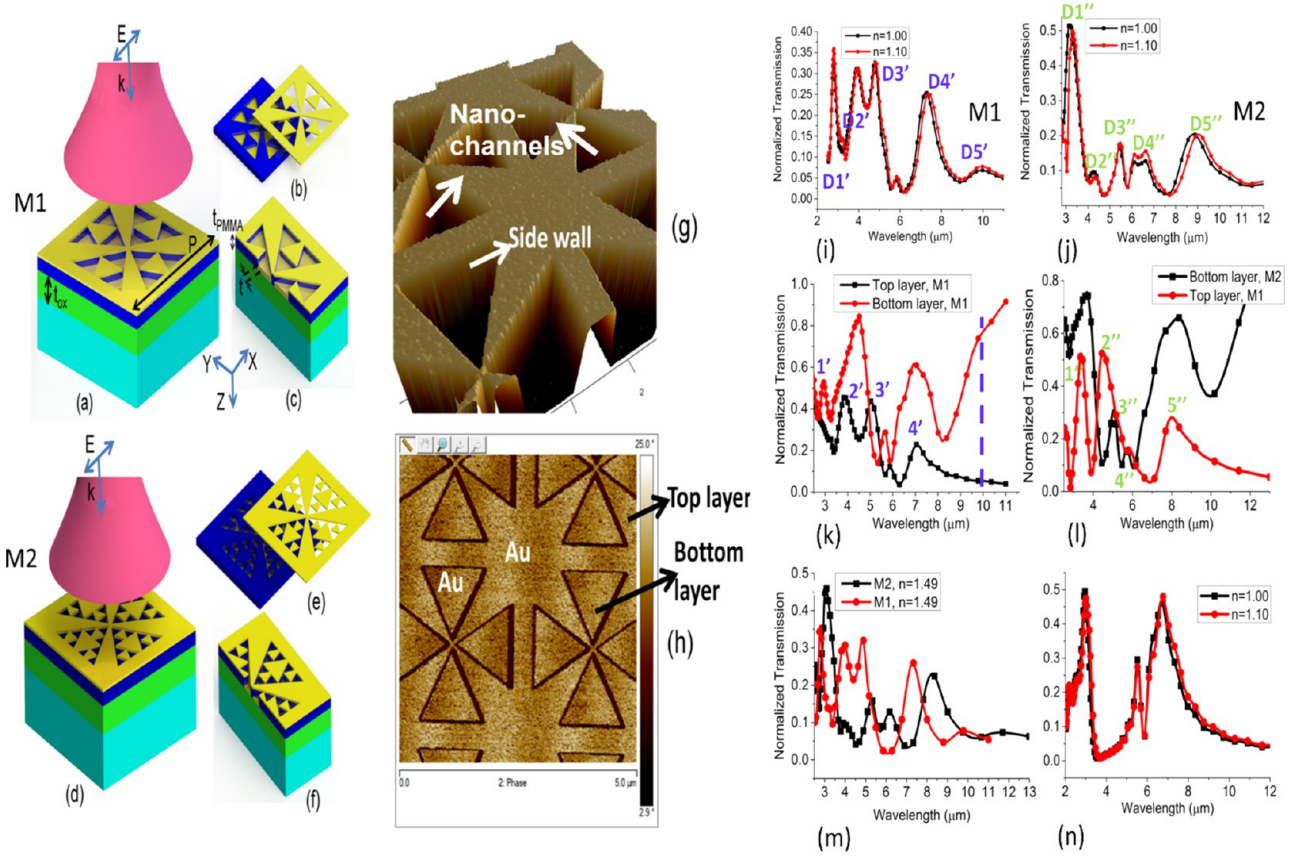

Figure 3. (a) 3D schematic of the M1 device; (b) merging top and bottom layouts of the first order; (c) cross-section of the M1 device; (d) 3D schematic of the M2 device; (e) merging top and bottom layouts of the second order; (f) cross-section of the M2 device; (g) AFM height profile of the conventional bow-tie nanostructure in the quasi-3D configuration; and (h) AFM phase profile of the conventional structure showing the dual Au layers. The substrate is Si coated with 1 μm thick (t_{ox}) thermal oxide. PMMA thickness, t_{PMMA}, and gold thickness, *t*, are fixed at 180 and 35 nm, respectively, unless otherwise stated. Simulated broadband optical transparency peaks (i) M1 and (j) M2. Origin of the peaks from the top and bottom layers, (k) M1 and (l) M2. (m) Effect of the PMMA absorption peak at 5.79 μm. (n) Simulated transparency peaks of the quasi-3D conventional bow-tie nanostructure, without any patterns within the triangular apertures.

also to exploit the strong impact of lightening-rod-derived surface currents on the resonance properties. We further provide the split gap (*s*) to achieve a dramatic enhancement of resonance contrast and optical magnetism in the mid-IR region, as discussed in the following sections. Note that through such a modified fractalization process with a recursively changing

DOI: 10.1021/acsomega.6b00201
ACS Omega 2016, 1, 818−831

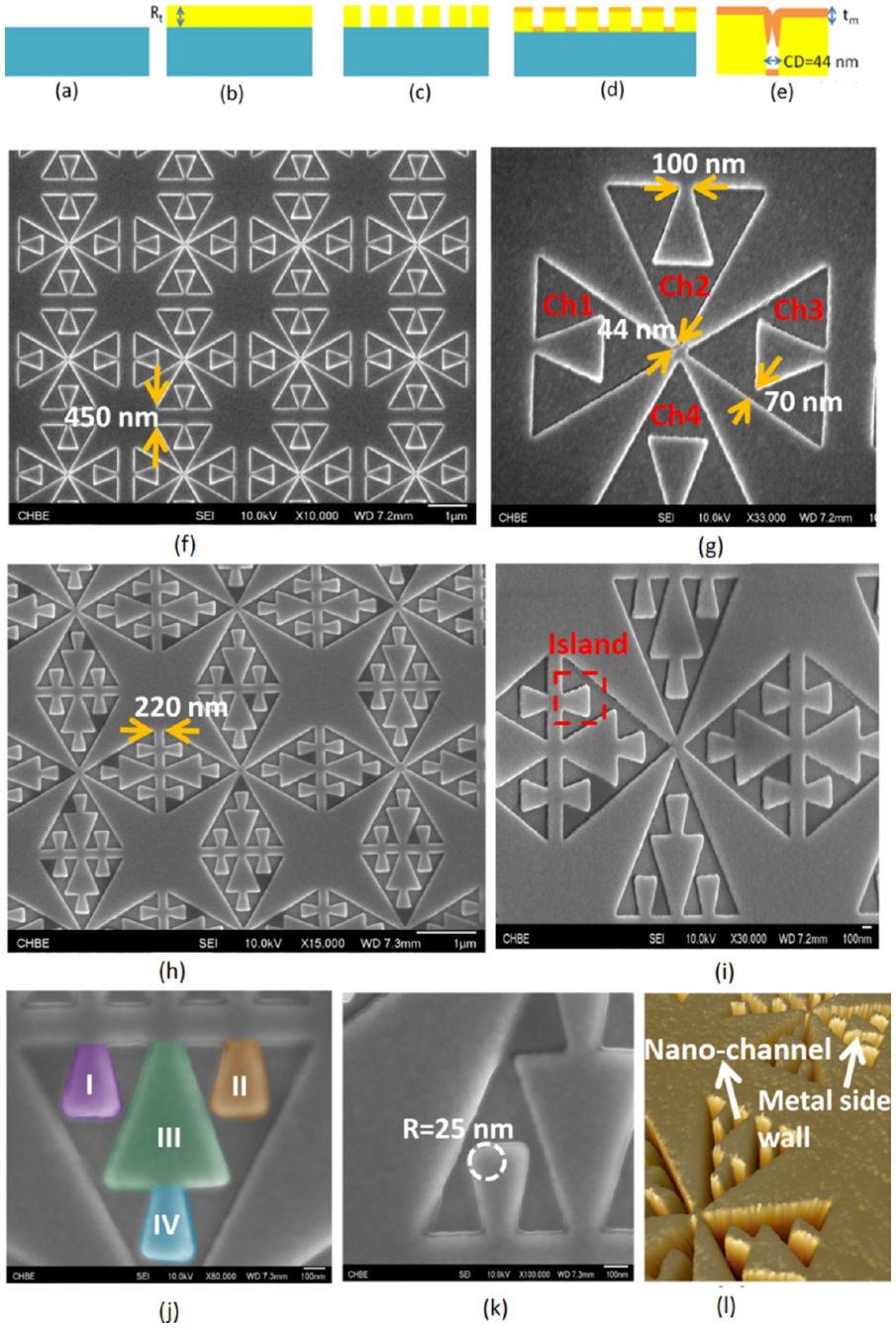

Figure 4. (a–d) Simplified process flow. (e) Issue of CD and side walls due to the shadowing of metal evaporation. R_t is the e-beam resist thickness, and t_m is thickness of the gold layer. (f) Dense array of the first-order device (M1). (g) Zoomed-in view of the M1 unit cell. (h) Dense array of the second-order device (M2). (i) Zoomed-in view of the M2 unit cell. (j) False-color SEM image illustrating the triangular islands obtained by the modified principle of *Sierpiński* fractal after the second iteration. (k) Roundedness of the corners due to e-beam backscattering. (l) AFM image of the metal side walls observed in the M2 device. Quasi-3D nanochannels are formed as the complementary and noncomplementary layouts of M2 are merged to each other, with self-alignment. The formation of nanoislands is indicated by the red dashed rectangle.

Haudsoff dimension we still achieve the coherently coupled self-symmetric radiators as numbered in Figures 1i and 2j. The height of the each host triangle is kept constant at 1.225 μm, roughly calculated from the half-wavelength dipole equation defined as $\lambda/2 = L$, where L is the total length of the dipole under a given polarization. Please note that because of the cross-coupled arrangement the resonance characteristics of the patterns do not critically depend on the polarization, albeit the profiles of the near-field enhancement can differ. Then, we obtain the complementary first-order fractal surface, as shown in Figure 1m, by subtracting the noncomplementary one from the uniform metal surface according to the Babinet principle. In the case of the second-order (M2) device, we follow the same design rules and obtain the complementary pattern, as shown in Figure 1p. The radiators in the noncomplementary surfaces thus appear as subwavelength apertures in the complementary surfaces, which are indicated in Figure 1m,p. A commercial 3D finite-difference time-domain (FDTD) solver (Lumerical) has been deployed on a 16 core, 2.60 GHz Intel Xeon ES-2670 (64 GB memory) processor to simulate the transmission spectrum

DOI: 10.1021/acsomega.6b00201
ACS Omega 2016, 1, 818–831

at near field under x-polarized plane waves incident normally. The near-field transmittance and reflectance have been captured by a transmission monitor and reflection monitor, respectively, both placed 15 μm away from the metal patterns. The simulation region has been terminated by periodic boundary conditions along the x and y directions and a perfectly matched layer along the z direction. A spatial resolution of dx = 1 nm, dy = 1 nm, and dz = 1 nm is chosen for accurate meshing. Optical properties of gold have been extracted from Palik. In Figures 2a and 1d, we mark the resonances supported by the complementary and noncomplementary surfaces in the simulated transmission spectra. As suggested by the Babinet principle, the observed transmission peaks of the complementary surface correspond to the transmission dips of the noncomplementary surface. However, among the three distinct resonances of M1, resonance I originates because of the complex interplay of the multiple resonance paths.[39−41] The sharp linewidth of this resonance can be explored further in the future study. On the contrary, resonance II is purely dipolar and resonance III is purely magnetic in the noncomplementary M1 surface. The magnetism at resonance III appears because of the presence of the split gap in the noncomplementary M1 layout and is associated with electric field enhancement at the split gap, as shown in Figure 1a. The corresponding transmission peaks of the complementary M1 surface along with the corresponding electric field distributions are shown in Figure 2b. Similarly, we observe a new set of resonances along with the additional magnetic resonances supported by the M2 patterns. The results along with the corresponding electric field distributions are shown in Figure 2c,d. The consistent contrast in the electric field distributions in Figure 2a,b and c,d is in strong agreement with the Babinet principle. From the simulation results, it becomes obvious that spatially and spectrally variant dipolar and magnetic modes can be sustained in the different orders of fractal-derived patterns.

Construction of the Quasi-3D Structures. Here, we propose the idea of self-aligned vertical integration of complementary and noncomplementary patterns for resonant optical transmission across a wide band not only to scale down the size of the footprint but also to bypass the challenge of nanometric alignment and topology in realizing multilayer nanostructures.[42,43] Figure 3a,d shows conceptual 3D schematics of the proposed idea. Figure 3b,e shows an exploded view of the two patterns coupled to each other through the poly(methyl methacrylate) (PMMA) spacer. The cross-sections of the devices are shown in Figure 3c,f. The atomic force microscopy (AFM) height profile of a conventional bow-tie aperture without any fractal inclusion in Figure 3g illustrates the 3D nature of the configuration and the formation of metal side walls during the process. We further extract the phase profile in Figure 3h and indicate the presence of bottom and top metal layers.

Evolution of the Broadband Optical Transparency Peaks. Figure 3i,j shows the transmission peaks supported by the M1 and M2 devices, respectively. The refractive index of PMMA has been modeled in the mid-IR range, considering the C═O vibrational peak at 5.79 μm.[44] The other weaker C−H peaks around 6−8 μm have been ignored in this work.[44] The refractive indices of Si and SiO_2 are set to be 3.47 and 1.45. We use the prime (′) and the double prime (″) symbols to distinguish between the first- and the second-order layouts, respectively. It can be observed that both of the configurations preserve five distinct peaks (D1′−D5′ and D1″−D5″) across the whole spectrum. The feature observed between D3′ and D4′, at around 5.79 μm, can be termed as the absorption-induced transparency (AIT) peak, which is a recent phenomenon of quantum electrodynamics.[45,46] We analyze the complex devices by subdividing them into two layers: top and bottom, as shown in Figure 3b,e. However, the presence of the PMMA framework and substrate can cause strong modulations of the resonances coming from both the layers. Hence, while simulating the top layer, the PMMA template is still attached at the bottom to take the refractive-index-induced shift into account, and while simulating the bottom layer, the substrate along with the oxide layer atop is not removed. Our proposition is that the transmission peaks from the top and bottom layers can be superimposed on each other without causing significant interference due to the shift caused by the presence of the PMMA spacer. We present the layer-specific peaks from M1 and M2 obtained by such a simulation in Figure 3k,l, respectively, and tag them with a number corresponding to a particular resonance peak in Figure 3i,j, respectively. It is observed that the peaks from the original devices can be roughly approximated by superimposing the peaks from the top and bottom layers, although a strong coupling-induced redshift and a change in peak intensity are observed.[47] Interestingly, the weak D5′ resonance in Figure 3i cannot be ascribed to any layer-specific peak. Rather, it is an outcome of strong coupling between the two layers around the wavelength marked by a dashed line in Figure 3k. The AIT peak between D3′ and D4′ and the transmission dip between D3″ and D4″ can be double-confirmed by the simulation results in Figure 3m, in which the vibrational mode of the PMMA is artificially removed. The structural dependence of the AIT phenomenon can be further verified from the transmission spectrum in Figure 3n of a conventional bow-tie structure in a quasi-3D configuration, as shown in Figure 3g,h. More importantly, the series of resonance peaks disappears in Figure 3n when the fractal patterns are excluded. The sensitivity of the resonance peaks supported by the quasi-3D structures can be confirmed from the simulation results in Figure 3i−k when the background refractive index is increased by 10%.

Fabrication and Characterization. The simplified process flow of the fabrication is shown in Figure 4a−e. A PMMA e-beam resist of thickness R_t is spin-coated on a clean oxide substrate. We consider three different values of R_t (110, 180, and 250 nm) to study the coupling between the top and bottom layers. However, increasing R_t can strongly affect the fidelity of the sharp corners of the fractals due to the increased forward scattering range parameter of the e-beam. The nanopatterns are obtained with a high-resolution 100 kV ELS-7000 Electron Beam Lithography equipment using raster scanning. The e-beam current is maintained at 200 pA. No proximity correction or indium tin oxide charge compensation layer has been considered for the current batch of chips. The development time is controlled at 70 s in a 1:3 methyl isobutyl ketone/isopropanol solution. Finally, a 5 nm thick Cr layer, followed by a 35 nm thick gold layer, is deposited by the Denton Explorer e-beam evaporator. Metal side walls as shown in Figure 4e can be present due to the shadowing effect, requiring careful optimization between the metal thickness (t_m) and critical dimension (CD) for successful implementation of the complex quasi-3D nanostructures. We repeatedly obtain a minimum feature size of 44 nm, as shown in Figure 4g, whereas the total metal thickness remains fixed at 40 nm. Note that such

DOI: 10.1021/acsomega.6b00201
ACS Omega 2016, 1, 818−831

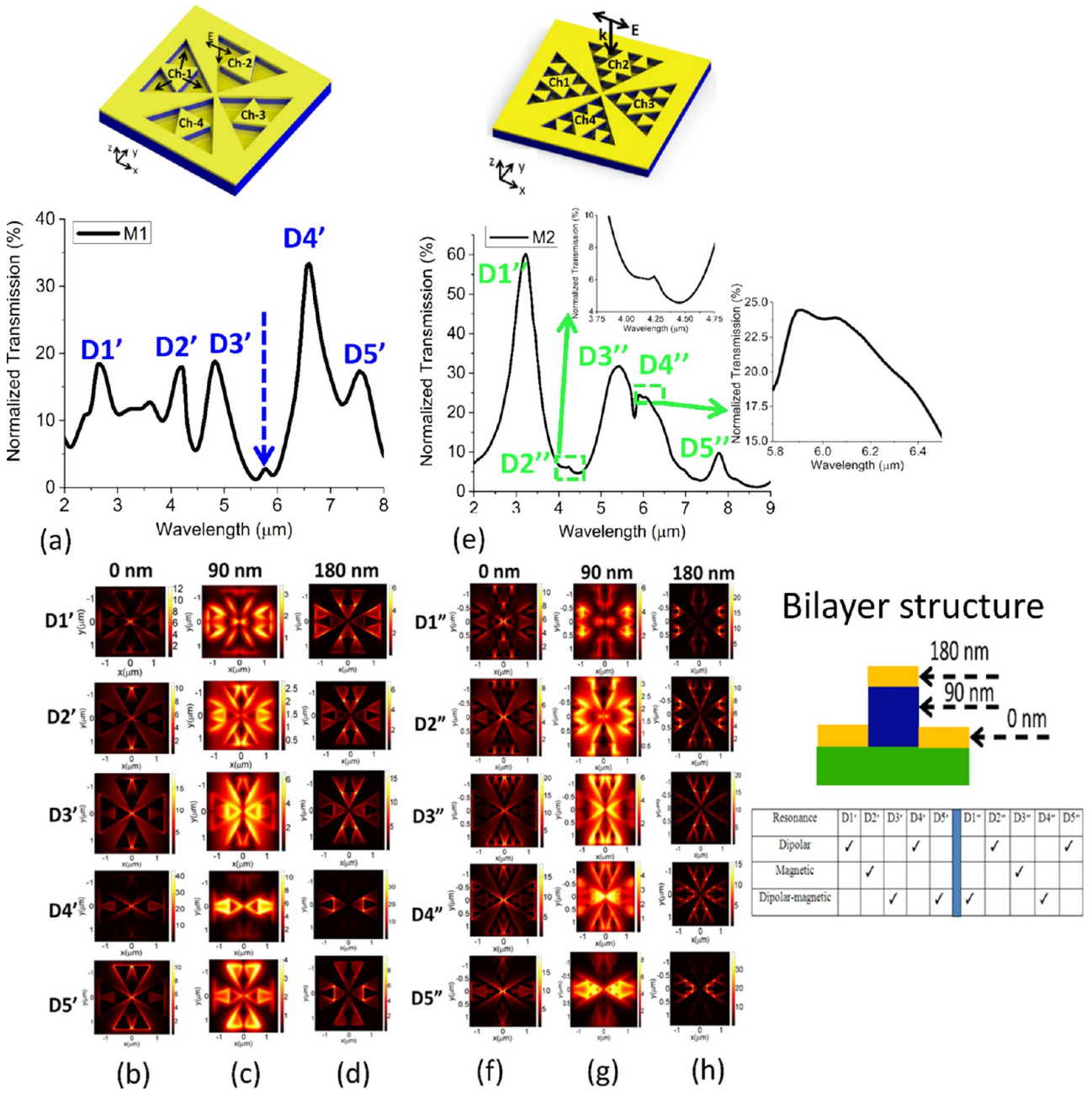

Figure 5. Proof-of-concept experimental demonstration of the broadband EOT-like peaks supported by the quasi-3D (a) M1 device and (e) M2 device. The inset shows a zoomed-in view of the weak features of the spectrum. Resonant electric field distribution for M1 at different heights: (b) 0 nm, (c) 90 nm, and (d) 180 nm. Resonant electric field distribution for M2 at different heights: (f) 0 nm, (g) 90 nm, and (h) 180 nm. The table in the inset shows a classification of the resonances depending on their mode of excitation.

a side wall can strongly affect the broadband resonances by introducing constant damping into the cavity system partially formed by the two self-aligned reflecting layers. Figure 4f,h shows the scanning electron microscopy (SEM) images of the large-area nanopatterns of orders 1 and 2 obtained by field-emission SEM. The zoomed-in view of the unit cells are shown in Figure 4g,i. Because of the 3D topography, we observe strong secondary electron emission from the edges of the geometries. The false-color SEM in Figure 4j illustrates the multiple resonance paths of the second-order fractal. After careful inspection, we observe strong backscattering-induced roundedness of the fractal corners, as shown in Figure 4k, which can cause deviation of the experimental results from the simulation results to some extent. Finally, the 3D metal side walls have been investigated using a Bruker AFM with a Si tip of 5 nm radius. The results have been postprocessed by NanoScope Analysis and illustrated in Figure 4l.

Normalized transmission and reflection spectra have been obtained on a broadband Agilent Fourier transform infrared (FTIR) spectrometer. The area of the aperture is considered to be 100 μm × 100 μm. The reflectance of the devices is normalized with respect to that of a smooth gold surface, and the transmittance is normalized with respect to the free-space transmission of light. The size of the aperture was adjusted carefully to match the size of each square pattern, thus eliminating the background reflection. The sampling resolution

DOI: 10.1021/acsomega.6b00201
ACS Omega 2016, 1, 818−831

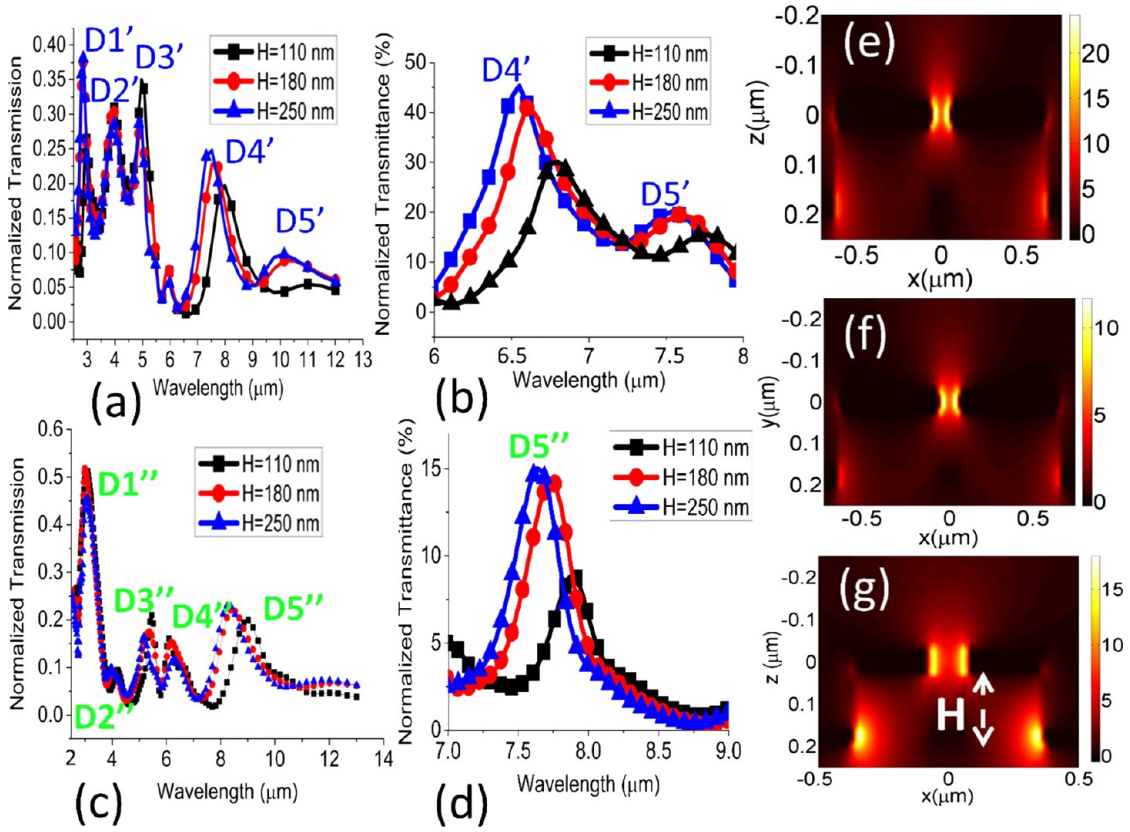

Figure 6. Effect of coupling distance (H) on the resonance characteristics of M1: (a) simulation, (b) experiment. Effect of coupling distance on the resonance characteristics of M2: (c) simulation, (d) experiment. Vertical coupling of the electric field at (e) D4′, (f) D5′, and (g) D5″ resonances. Cross-sectional plane of (h) M1 and (i) M2 devices, where the electric field distributions are plotted. Resonances D4′, D5′, and D5″ are found to be the most strongly influenced by the coupling distance in the experiment.

is maintained at 4 cm^{-1} to minimize the presence of water absorption peaks, although the CO_2 peak at 4.26 μm can appear in the spectrum, depending on the ambient concentration. The mirror repetition rate is fixed at 40 kHz, and the number of scans is maintained at 64.

RESULTS AND ANALYSIS

Proof-of-Concept Demonstration. Figure 5a,e shows a proof-of-concept demonstration of broadband mid-IR transmission peaks supported by fractal devices. The corresponding reflection dips for the M1 and M2 patterns are provided in the Supporting Information for further verification (Figures S1 and S2). It has been found that the resonant transmittance can reach up to 50% (D1″) in the far-field measurement in an otherwise opaque medium. Such a level of EOT-like transmission despite the presence of a bottom layer indicates the potential for resonance-based applications of the devices in the transmission mode. Also note that the conventional bow-tie structure in the quasi-3D configuration can only support two modes within the range of interest. On the other hand, the fractal patterns can support at least five distinct resonances, as predicted by the 3D FDTD simulation results in Figure 3i,j. Several weak features such as the D2″ resonance with a kink, the minor dip around the D4″ region, and the presence of the D5′ shoulder are exactly captured by the highly sensitive LN_2-cooled HgCdTe detector of the FTIR spectrometer. The appearance of the AIT peak is also obvious in Figure 5a, as indicated by the dashed line. The experimental reflection and transmission spectra of the PMMA thin film are provided in Figures S3 and S4. The transmission dip around the C═O transition clearly confirms the existence of the AIT peak supported by the M1 device. Here, we classify the five resonances of each of the devices on the basis of their spatial nature at the bottom plane. A bow-tie triangle can exhibit transverse (dipolar) and longitudinal resonances of different orders in its conventional shape. Because of the presence of the split gap, we also expect the magnetic resonance in a modified form while the dipolar effect exists. Figure 5b–d,f–h shows the electric field distribution at three different planes (0, 90, and 180 nm) of the M1 and M2 devices, respectively. By tracking the location of the peak electric field at the bottom plane, we classify the resonances as dipolar, magnetic, and dipolar–magnetic in the table of Figure 5(inset). The field profiles at the top plane (180 nm) clearly indicate the hotspots available in the corners of the modified fractal layouts across a broad range of wavelengths, which are formed by the enhanced lightening-rod effect of the fractal patterns. Such hotspots are potentially useful for chemical-specific dielectrophoretic sensing in the mid-IR range. On the contrary, a complex transformation of the phase and intensity of the electric fields occurs along the depth direction. Such field transformation in a thin region opens up a new avenue for volumetric refractive index sensing of solutions. We further demonstrate high-fidelity fabrication of the proposed nanostructures. There exist two nanoscale parameters, f and s, in the noncomplementary fractal patterns for the precise tuning of resonance characteristics. The key mechanism of tuning the dipolar modes lies in engineering the surface current so as to manipulate dipolar moment **p**, defined as[48]

DOI: 10.1021/acsomega.6b00201
ACS Omega 2016, 1, 818–831

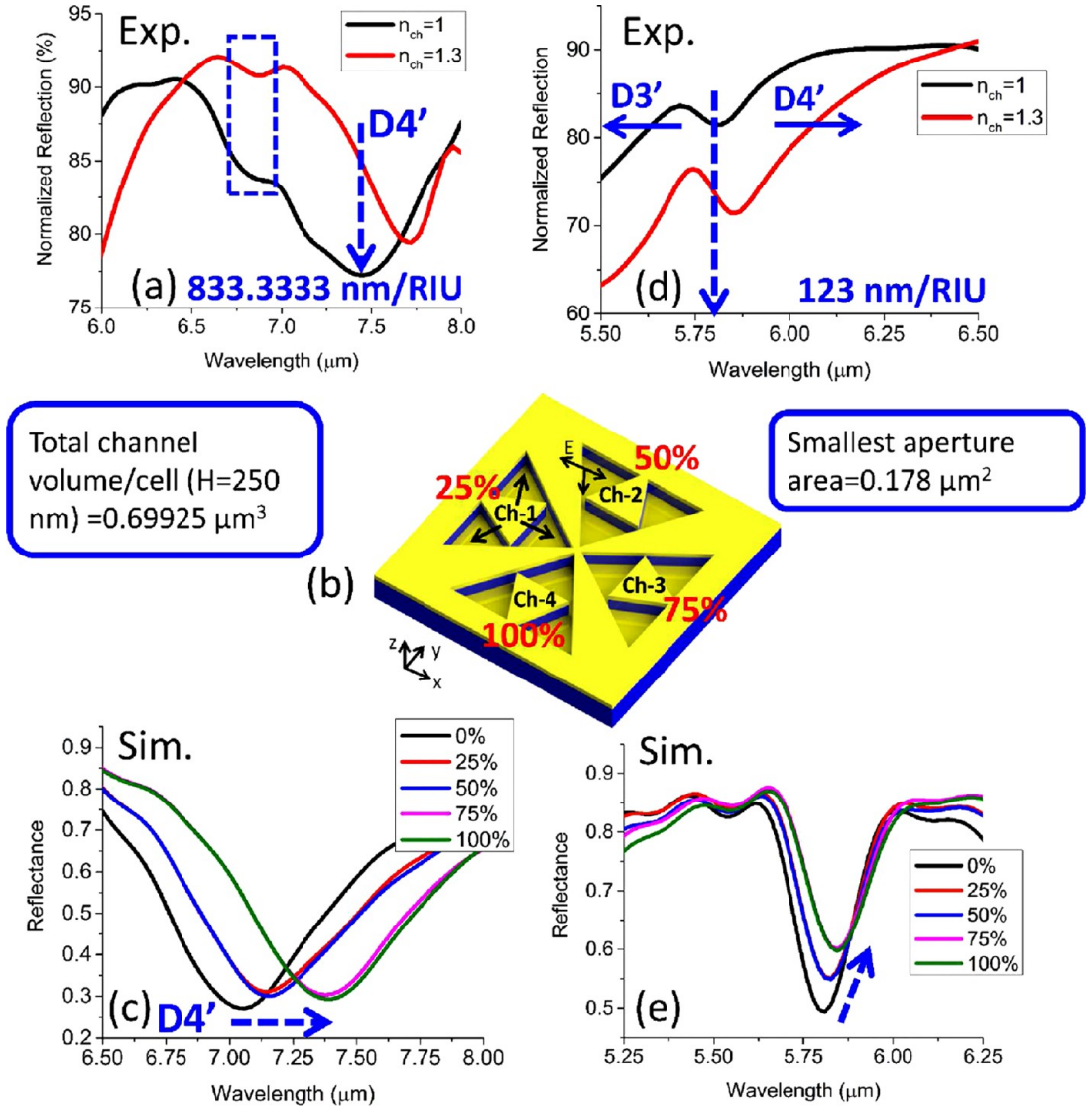

Figure 7. Volumetric refractive index sensing for the M1 structure. Experimental shifts in the (a) D4′ resonance, (d) the hybridized feature between the D3′ and D4′ resonances, (b) the distribution of the volumetric nanochannels in the M1 device along with the total channel volume and smallest aperture area. Simulated evolution of the wavelength shifts as the channels are sequentially infiltrated: (c) D4′ resonance and (e) hybridized feature between the D3′ and D4′ resonances. The dashed arrows indicate the spectral locations of the features and modulation of the spectrum. The dashed rectangle indicates the presence of the feature that possibly originates because of the structural imperfection of the nanostructures and cannot be captured by the simulation model. The refractive index of water is assumed to be 1.3 at the mid-IR spectrum for the simulation.[52]

$$\mathbf{p} = \frac{1}{-j\omega}\int_V J(x, y, z)\, dV \tag{1}$$

Here, J is the polarization current density determined by the displacement field and electric field of the structure. Parameter f can strongly affect the moment, as it will alter the charge density at the junctions of the fractal patterns. Parameter s is essential here to enforce all of the constituent radiators to supplement the surface current at the acute junctions. Besides, s will allow the magnetic resonance whose wavelength is defined as $\lambda \propto \sqrt{LC}$, where L and C are the inductance and capacitance of the structure, respectively. The intensity of the magnetic resonance is proportional to the magnetic moment $\mathbf{m}$, defined as[48]

$$\mathbf{m} = \frac{1}{2}\int_V r' \times J(r')dV \tag{2}$$

On the basis of the Babinet principle, it is obvious that f and s will have equivalent impacts on the complementary surfaces. Thus, f and s can reasonably engineer the resonance intensity and location of the actual 3D fractal devices by the strong manipulation of moments. We show the simulation and experimental results of M1 in Figure 6a–d as parameters f and s are varied. Despite the presence of a metal side wall, we observe a good agreement between the simulation and experimental results. For instance, a consistent increase in the D4′ and D5′ intensities is observed as parameter f is increased, which is in agreement with simulation. In contrast to that in f, the variation in s does not yield a noticeable change in the intensity and location of the resonances both in the simulation and in the experiment. Similarly, for the M2 design, the role of f in altering the resonance characteristics is found to be more dominant than that of s both in the simulation and in the experiment (Figure S5d–g). A rather detailed analysis of such a variation can be found in the Supporting Information (Figures

DOI: 10.1021/acsomega.6b00201
ACS Omega 2016, 1, 818–831

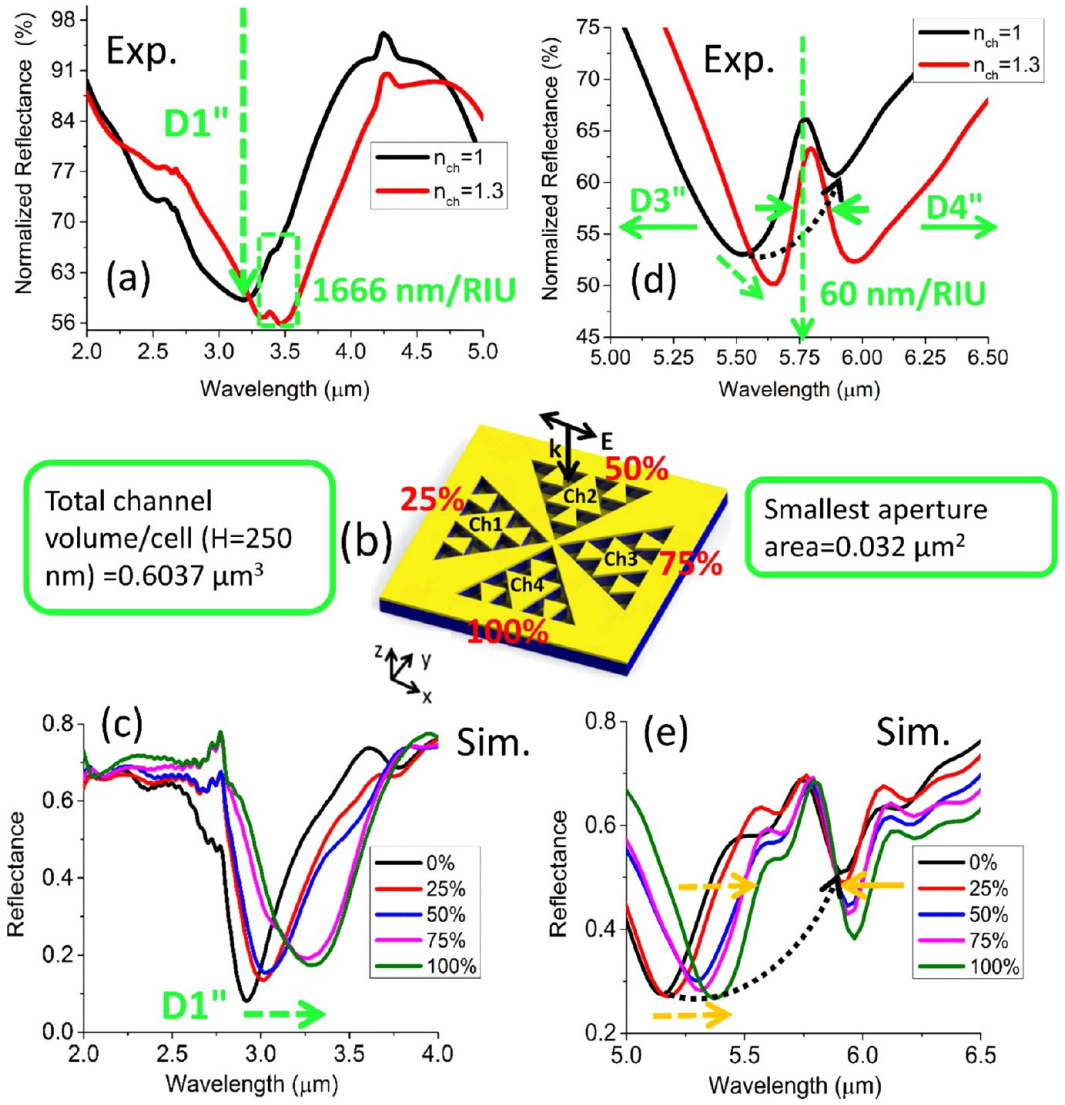

Figure 8. Volumetric refractive index sensing for the M2 structure. Experimental shifts in the (a) D1″ resonance, (d) the hybridized feature between the D3″ and D4″ resonances, and (b) the distribution of the volumetric nanochannels in the M2 device along with the total channel volume and smallest aperture area. Simulated evolution of the wavelength shifts as the channels are sequentially infiltrated: (c) D1″ resonance and (e) the hybridized feature between the D3″ and D4″ resonances. The narrowing of the quality factor of the feature is observed both in the experiment and in the simulation, which can be partly attributed to the redshift of the adjacent D3″ resonance, as indicated by the black dotted line. The green dashed arrow indicates the spectral locations of the features and modulation of the spectrum. The green dashed rectangle indicates the presence of the weak D2″ feature, which overlaps with the D1″ mode as the wavelength shift occurs. The refractive index of water is assumed to be 1.3 at the mid-IR spectrum for the simulation.[52]

S6–S9). The results indicate a high repeatability and control of the fabrication process for the reversed-engineered nanostructures in the presence of multiple practical issues, for example, e-beam scattering and charging and side walls.

Vertical Coupling of Quasi-3D Nanostructures. Figure 6e–g shows the vertical coupling along the *xz* plane through the $y = 0$ line for the strongly coupled resonances: D4′, D5′, and D5″, respectively. We study the role of such coupling by varying the spacing (H) as determined by the PMMA thickness during fabrication. Three different thicknesses, 110, 180, and 250 nm, have been considered. Note that at a higher PMMA thickness pattern distortion can be crucial because of the increased forward scattering of the e-beam. On the other hand, at a lower thickness, the metal side wall issues could be even more complicated because of the possible shortening of the top and bottom layer by the shadowing effect. Nevertheless, the results in Figure 6a–d show strong agreement between simulation and experiment for the strongly coupled resonances. We observe a strong redshift as the spacing is decreased, which can be explained by treating the coupled metal–dielectric–metal system as an optical circuit.[49] As the spacing is decreased, the capacitance induced between the two metal layers is increased. This can yield a longer resonance wavelength, as predicted by $\lambda \propto \sqrt{LC}$. An intensity change is also observed as the spacing is changed, again indicating the role of vertical coupling in the resonant conditions of the transmission peaks. Such a unique design freedom of the proposed quasi-3D devices makes them potentially useful for ultracompact sensors in massively parallel and broadband applications. In particular, pixelated thermal imaging devices require highly scalable multispectral unit cells, while minimizing the usage of the chip real estate. Thus, the vertical coupling-mediated height

DOI: 10.1021/acsomega.6b00201
ACS Omega 2016, 1, 818–831

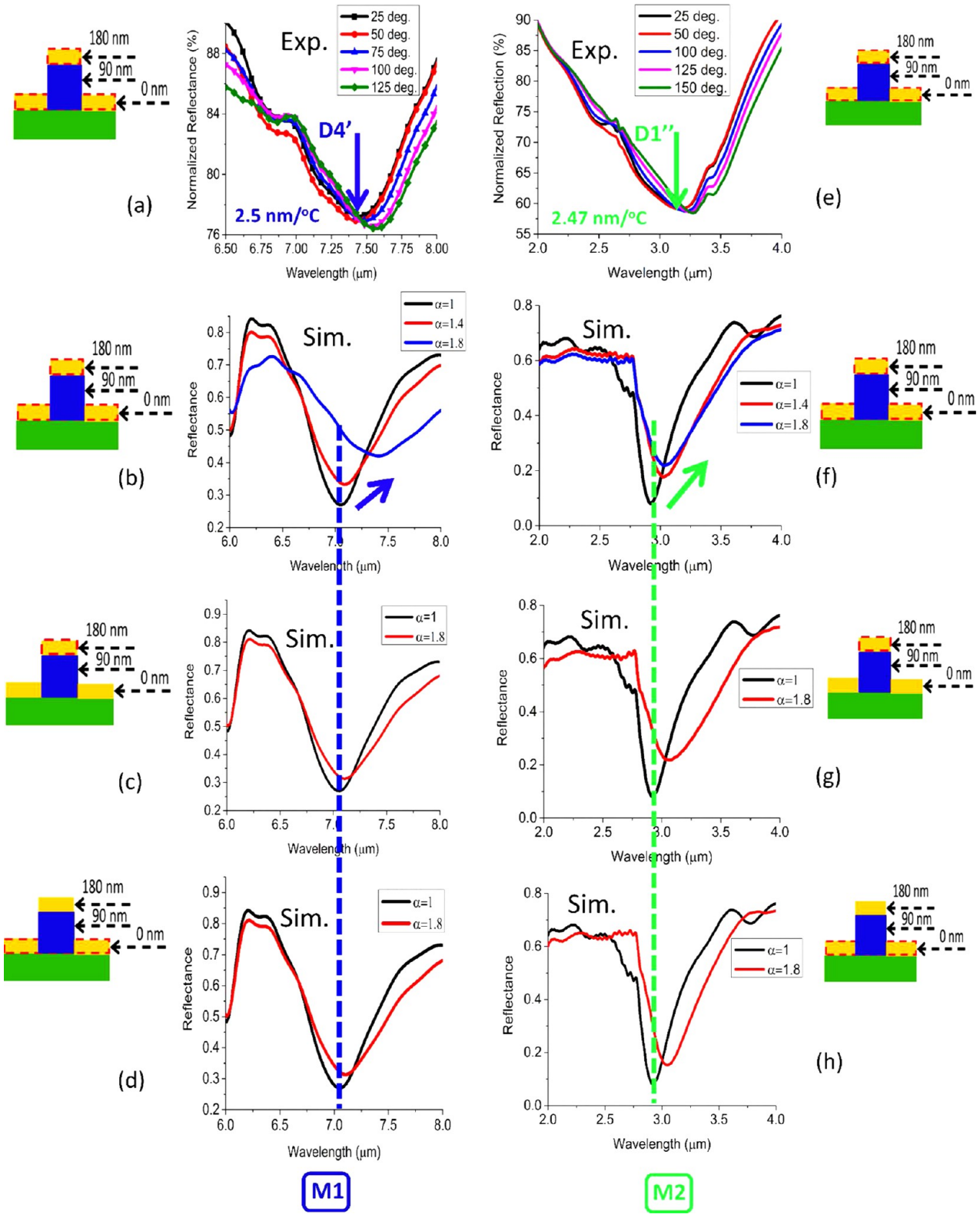

Figure 9. Thermal responses of the bilayer plasmonic metasurfaces. Experimentally observed shifts of the pure plasmonic modes caused by resistive heating of the metal: (a) D4′ resonance in M1, (e) D1″ resonance in M2. Simulated shifts when both layers are assumed to be heated: (b) D4′ resonance in M1 and (f) D1″ resonance in M2; when the top layer is heated: (c) D4′ resonance in M1 and (g) D1″ resonance in M2; and when the bottom layer is heated: (d) D4′ resonance in M1 and (h) D1″ resonance in M2. The solid arrows indicate the spectral locations of the features and modulation of the spectrum. The red dashed rectangle indicates the region that is assumed to be heated. The dashed lines indicate the reference position when no heating is assumed in the simulation.

dependence of the fractalized quasi-3D surfaces will be technologically important for harnessing a broad range of useful black-body radiations (3−12 μm) on a significantly reduced footprint area.

DOI: 10.1021/acsomega.6b00201
ACS Omega 2016, 1, 818−831

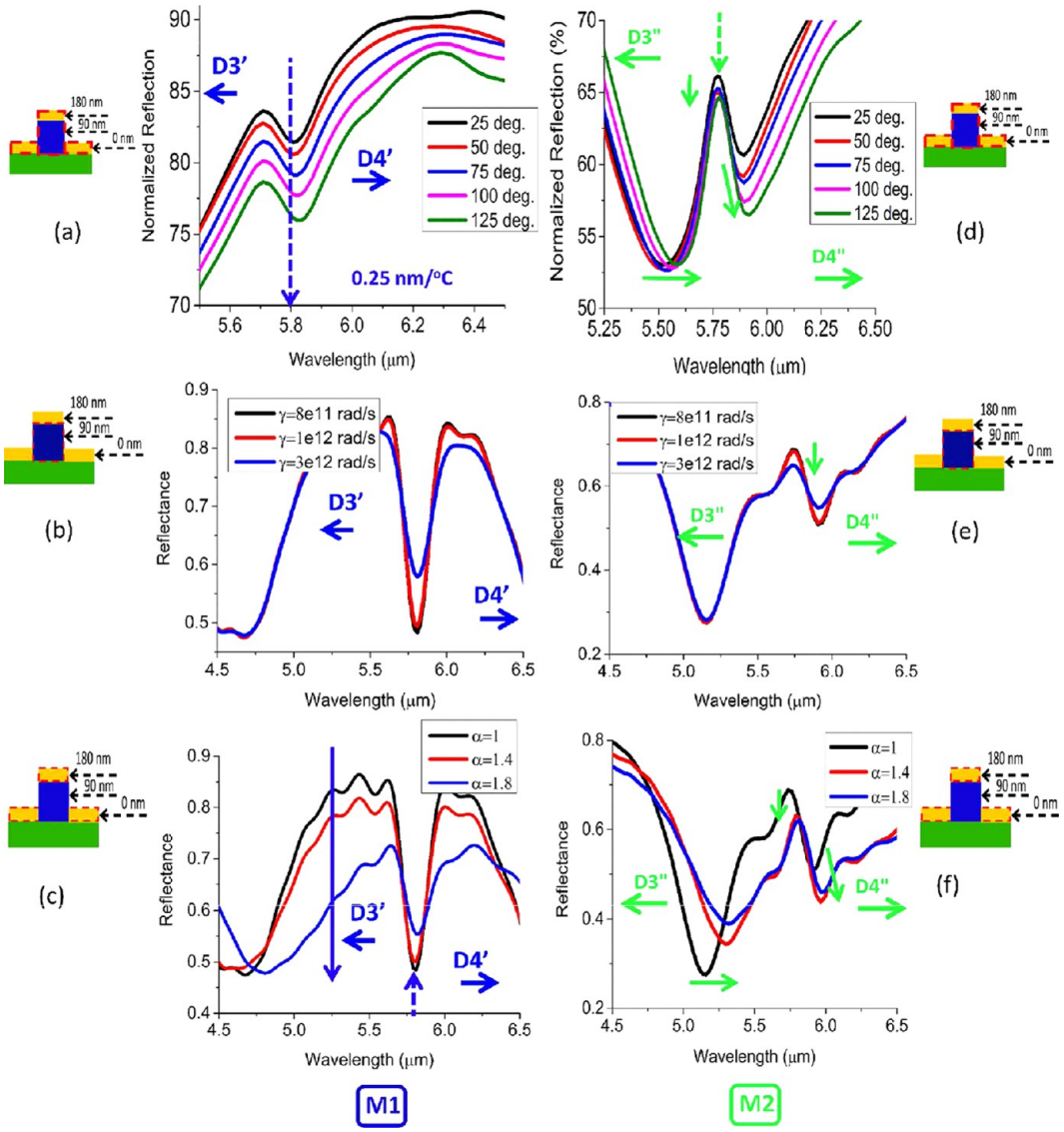

Figure 10. Thermal responses of the bilayer plasmonic metasurfaces. Experimentally observed shifts in the hybridized modes caused by resistive heating of the metal and broadening of the PMMA vibrational absorption: (a) M1 and (d) M2. Simulated shifts when only PMMA is heated: (b) M1 and (e) M2 and when the metal layers are heated: (c) M1 and (f) M2. The dashed arrows indicate the spectral locations of the features in the spectra. The solid arrows indicate modulation of the spectra in terms of intensity variation and wavelength shift.

Volumetric Refractive Index Sensing. The proposed fractal architectures can be treated as a novel platform for multiple analyte SEIRA, which is a powerful biomedical analysis tool.[50,51] The quasi-3D nanochannels of the nanostructures in which volumetric enhancement of the electric field occurs can be potentially useful for such applications. Herein, because of the hybrid nature of the devices, we consider both purely plasmonic modes (D4′ and D1″) and the hybridized features (between D3′ and D4′ and between D3″ and D4″) and demonstrate their volumetric refractive index sensitivity in the reflection mode. After carefully rinsing in deionized water, the samples are quickly tested to observe the incurred wavelength shift. We calculate refractive index unit (RIU) shifts of 833.3333 and 123 nm for the plasmonic mode and hybridized mode of the M1 device, respectively, as shown in Figure 7a,d. Note that the PMMA was hard-baked before metal deposition and the spectrum reverts to its original position after drying in N_2 flow. Thus, the influence of soaking by PMMA can be safely ignored in this case. We further attempt to understand the contribution of the light−matter interaction inside the nanochannels shown in Figure 7, totaling a volume of 0.69925 μm^3 per unit cell, while having a minimum aperture area of 0.178 μm^2. As observed in Figure 7c,d, a monotonic increase in the wavelength shift persists when the four channels are sequentially infiltrated (25, 50, 75, 100%) under a given polarization. We conduct a similar experiment for the M2 device, which has a total channel volume of 0.6037 μm^3 per unit cell, while the minimum aperture size is now reduced to 0.032 μm^2. The RIU shift calculated from Figure 8a,d becomes 1666 and 60 nm for the purely plasmonic mode and hybridized mode, respectively. The ∼2 times increase in the shift of the plasmonic mode can be justified by the enhanced modulation observed in the simulation results in Figure 8c, where the nanochannels are assumed to be infiltrated sequentially. Under a given polarization, a noticeable cross-coupling is also observed as the sample infiltration increases from 25 to 50% or from 75 to 100%. Considering a less volume of interaction in the second-order design, such enhanced sensitivity can be

DOI: 10.1021/acsomega.6b00201
ACS Omega 2016, 1, 818−831

qualitatively attributed to the complexity of the light−matter interaction within the unit cell. On the other hand, the hybridized mode undergoes a narrowing, followed by a shift, as shown in Figure 8d. This is caused by the shift of the background plasmonic mode, as indicated by the dotted arrow in Figure 8d,e. The coupling between the plasmonic mode and PMMA absorption is also changed due to the presence of water.[53]

Thermoresponsive Characteristics. Finally, we demonstrate a reversible thermoresponsive tuning mechanism for the quasi-3D structures by relying on the permittivity change of the metal with temperature. We propose that bilayer metallic structures can obtain better thermoresponsive characteristics as compared to those of single-layered devices. Such an improvement will be mainly mediated by vertical coupling, as demonstrated in the previous section. The temperature dependence of metal permittivity is incorporated into the simulation by the modified Drude model, as below[54]

$$\varepsilon = 1 - \frac{\omega_p^2}{\omega^2 + i\alpha\Gamma\omega} \quad (3)$$

Here, ω_p is the plasma frequency, Γ is the Drude damping parameter, and α is the factor to quantify the increase in damping as the temperature is increased. The nominal values of ω_p and Γ are set at 9 and 0.07 eV, respectively, in the unit of energy. A temperature increase by 100° is considered in this work. Therefore, the change in real part of the PMMA refractive index can be safely ignored.[55] However, thermal broadening of PMMA absorption can occur according to the power law for the vibrational mode, defined as $\gamma(T) \propto T^n$, where γ is the linewidth, T is the temperature, and exponent n is greater than 1.[56] For the measurement, the sample is placed on a heating stage, which is capable of heating up to 450 °C. The temperature of the stage is controlled by a temperature controller, with a variation of less than 5%. The sample chamber is properly insulated from the ambience. Measurements are taken 5 min after the stable reading of a particular temperature is reached. In the current setup, only the reflection signal can be captured while the heating stage is incorporated. Temperature-induced shifts of ∼2.5 and 2.47 nm/°C are experimentally observed in Figure 9a,e for the purely plasmonics modes D4′ and D1″, respectively. The shifts obtained are at least 14.3 times better than those from the previous thermoplasmonic sensor, which we attribute to the vertical coupling in the bilayer structures. To understand the role of the bilayer structure, we conduct a detailed simulation in Figure 9b−d,f−h. It is clear from the results that the thermoresponsive behavior of the proposed nanostructures is concurrently aided by both the layers.

The individual effects of each metal layer in both the devices (M1 and M2) are evident from the simulation results presented in Figure 9c,d,g,h, where the layer-specific metal permittivity is selectively altered. Detailed investigation into the combined effect may further identify the contribution of vertical coupling in bilayer geometry toward the enhanced thermoresponsivity of the supported plasmonic modes.

Later, we consider the hybridized features as discussed previously in Figure 10a,d for thermal tuning. This time a shift of the hybridized feature is observed for the M1 case. For the M2 case, the shift in the background resonance mode is clearly observable. Note that the temperature dependence of these modes can be simultaneously associated with the permittivity change and linewidth broadening of PMMA, making it challenging to exactly reproduce the experimental observation in the simulation. Nevertheless, we attempt to decouple the two effects by the simulation results in Figure 10b,c,e,f. It becomes obvious that the shift and intensity variation observed in the experiment is significantly associated with the thermally driven reversible change in the metal permittivity. We believe that the enhanced thermoresponsive behavior of the structure in conjunction with mid-IR operation will pave the way for chemical-specific nanothermodynamic study of reactions.

CONCLUSIONS

In conclusion, we demonstrate a fractal-inspired quasi-3D platform for thermoresponsive, volumetric, and multispectral detection at the mid-IR spectrum in a small footprint. Fabrication of the nanoarchitectures relies on single-step lithography and therefore can be feasibly deployed for large-scale application. Enhanced electromagnetic properties, such as cross-coupling, optical magnetism, and the lightening-rod effect, have been critically considered for the development of the final layouts. We demonstrate the proof-of-concept by closely matching the experimental results with those from the simulation and performing extensive parameter variation. Furthermore, we successfully report vertical coupling to be an alternative pathway for ultimate miniaturization of quasi-3D devices. Finally, we demonstrate volumetric refractive sensing and enhanced thermoresponsive behavior of the nanostructures successfully. We believe that the proposed multispectral platform will establish a new avenue for dielectrophoretic cell study and thermoresponsive volumetric sensing in the chemically active mid-IR spectrum.

ASSOCIATED CONTENT

Supporting Information

The Supporting Information is available free of charge on the ACS Publications website at DOI: 10.1021/acsomega.6b00201.

Discussion on fabrication, simulations, and measurements and additional results (PDF)

AUTHOR INFORMATION

Corresponding Author

*E-mail: elelc@nus.edu.sg.

Author Contributions

D.H. carried out the electromagnetic designing, simulation, fabrication, and experiments. H.C.P. built the mid-IR characterization setup. C.L. conceived the experiments and planned and supervised them. All authors participated in the scientific discussions and reviewed the manuscript.

Notes

The authors declare no competing financial interest.

ACKNOWLEDGMENTS

The authors acknowledge the financial support from the research grant of MOE/NUS, ARF-Tier 2 (MOE2012-T2-2-154, NUS WBS: R-263-000-A59-112) “Monolithic integrated Si/AlN nanophotonics platform for optical NEMS and OEICs”, CRP-15th (NRF-CRP001-019) “Piezoelectric Photonics Using CMOS Compatible AlN Technology for Enabling The Next Generation Photonics ICs and Nanosensors”, CRP-08th “Energy Harvesting Solutions for Biosensors” at the National University of Singapore, and the partial support by National

DOI: 10.1021/acsomega.6b00201
ACS Omega 2016, 1, 818−831

Natural Science Foundation of China under Grant No. 61474078 at NUS (Suzhou) Research Institute, Suzhou, China.

REFERENCES

(1) Karker, N.; Dharmalingam, G.; Carpenter, M. A. Thermal Energy Harvesting Plasmonic Based Chemical Sensors. *ACS Nano* **2014**, *8*, 10953−10962.

(2) Dregely, D.; Lindfors, K.; Lippitz, M.; Engheta, N.; Totzeck, M.; Giessen, H. Imaging and steering an optical wireless nanoantenna link. *Nat. Commun.* **2014**, *5*, No. 4354.

(3) Hasan, D.; Ho, C. P.; Pitchappa, P.; Lee, C. Dipolar Resonance Enhancement and Magnetic Resonance in Cross-Coupled Bow-Tie Nanoantenna Array by Plasmonic Cavity. *ACS Photonics* **2015**, *2*, 890−898.

(4) Xu, X.; Hasan, D.; Wang, L.; Chakravarty, S. Guided-mode-resonance-coupled plasmonic-active SiO_2 nanotubes for surface enhanced Raman spectroscopy. *Appl. Phys. Lett.* **2012**, *100*, No. 191114.

(5) Ren, F.; Campbell, J.; Hasan, D.; Wang, X.; Rorrer, G. L.; Wang, A. X. In *CLEO: Science and Innovations*, Proceedings CLEO: 2013; OSA Publishing: San Jose, California, United States, June 9−14, 2013; pp 1−2.

(6) Albella, P.; Poyli, M. A.; Schmidt, M. K.; Maier, S. A.; Moreno, F.; Sáenz, J. J.; Aizpurua, J. Low-Loss Electric and Magnetic Field-Enhanced Spectroscopy with Subwavelength Silicon Dimers. *J. Phys. Chem. C* **2013**, *117*, 13573−13584.

(7) Albella, P.; Shibanuma; Shibanuma, T.; Maier, S. A. Switchable directional scattering of electromagnetic radiation with subwavelength asymmetric silicon dimers. *Sci. Rep.* **2015**, *5*, No. 18322.

(8) Caldarola, M.; Albella, P.; Cortés, E.; Rahmani, M.; Roschuk, T.; Grinblat, G.; Oulton, R. F.; Bragas, A. V.; Maier, S. A. Non-plasmonic nanoantennas for surface enhanced spectroscopies with ultra-low heat conversion. *Nat. Commun.* **2015**, *6*, No. 7915.

(9) Shibanuma, T.; Albella, P.; Maier, S. A. Unidirectional light scattering with high efficiency at optical frequencies based on low-loss dielectric nanoantennas. *Nanoscale* **2016**, *8*, 14184−14192.

(10) De Angelis, F.; Malerba, M.; Patrini, M.; Miele, E.; Das, G.; Toma, A.; Proietti Zaccaria, R.; Fabrizio, E. D. 3D Hollow Nanostructures as Building Blocks for Multifunctional Plasmonics. *Nano Lett.* **2013**, *13*, 3553−3558.

(11) Güngör, K.; Ünal, E.; Volkan Demir, H. Nanoplasmonic surfaces enabling strong surface-normal electric field enhancement. *Opt. Express* **2013**, *21*, 23097−23106.

(12) Virk, M.; Xiong, K.; Svedendahl, M.; Käll, M.; Dahlin, A. B. A. Thermal Plasmonic Sensor Platform: Resistive Heating of Nanohole Arrays. *Nano Lett.* **2014**, *14*, 3544−3549.

(13) Shen, Y.; Zhou, J.; Liu, T.; Tao, Y.; Jiang, R.; Liu, M.; Xiao, G.; Zhu, J.; Zhou, Z.; Wang, X.; Jin, C.; Wang, J. Plasmonic gold mushroom arrays with refractive index sensing figures of merit approaching the theoretical limit. *Nat. Commun.* **2013**, *4*, No. 2381.

(14) Gartia, M. R.; Hsiao, A.; Pokhriyal, A.; Seo, S.; Kulsharova, G.; Cunningham, B. T.; Bond, T. C.; Liu, G. L. Colorimetric Plasmon Resonance Imaging Using Nano Lycurgus Cup Arrays. *Adv. Opt. Mater.* **2013**, *1*, 68−76.

(15) Stewart, M. E.; Mack, N. H.; Malyarchuk, V.; Soares, J. A. N. T.; Lee, T.; Gray, S. K.; Nuzzo, R. G.; Rogers, J. A. Quantitative multispectral biosensing and 1D imaging using quasi-3D plasmonic crystals. *Proc. Natl. Acad. Sci. U.S.A.* **2006**, *103*, 17143−17148.

(16) Daqian, W.; Xinglong, Y.; Qiuming, Y. Tuning multiple Fano and plasmon resonances in rectangle grid quasi-3D plasmonic-photonic nanostructures. *App. Phys. Lett.* **2013**, *103*, No. 053117.

(17) Pan, L.; Park, Y.; Xiong, Y.; Ulin-avila, E.; Wang, Y.; Zeng, L.; Xiong, S.; Rho, J.; Sun, C.; Bogy, D. B.; Zhang, X. Maskless Plasmonic Lithography at 22 nm Resolution. *Sci. Rep.* **2011**, *1*, 1−6.

(18) Roxworthy, B. J.; Ko, K. D.; Kumar, A.; Fung, K. H.; Chow, E. K. C.; Liu, G. L.; Fang, N. X.; Toussaint, K. C. Application of plasmonic bowtie nanoantenna arrays for optical trapping, stacking, and sorting. *Nano Lett.* **2012**, *12*, 796−801.

(19) Kinkhabwala, A.; Yu, Z.; Fan, S.; Avlasevich, Y.; Müllen, K.; Moerner, W. E. Large single-molecule fluorescence enhancements produced by a bowtie nanoantenna. *Nat. Photonics* **2009**, *3*, 654−657.

(20) Sivis, M.; Duwe, M.; Abel, B.; Ropers, C. Extreme-ultraviolet light generation in plasmonic nanostructures. *Nat. Phys.* **2013**, *9*, 304−309.

(21) Roxworthy, B. J.; Bhuiya, A. M.; Inavalli, V. V.; Chen, H.; Toussaint, K. C. Multifunctional Plasmonic Film for Recording Near-Field Optical Intensity. *Nano Lett.* **2014**, *14*, 4687−4693.

(22) Volpe, G.; Volpe, G.; Quidant, R. Fractal plasmonics: subdiffraction focusing and broadband spectral response by a Sierpinski nanocarpet. *Opt. Express* **2011**, *19*, 3612−3618.

(23) Afshinmanesh, F.; Curto, A. G.; Milaninia, K. M.; Van Hulst, N. F.; Brongersma, M. L. Transparent Metallic Fractal Electrodes for Semiconductor Devices. *Nano Lett.* **2014**, *14*, 5068−5074.

(24) Abdellatif, S.; Kirah, K. Nanowire photovoltaic efficiency enhancement using plasmonic coupled nano-fractal antennas. *Opt. Lett.* **2013**, *38*, 3680−3683.

(25) Luchowski, R.; Shtoyko, T.; Matveeva, E.; Sarkar, P.; Borejdo, J.; Gryczynski, Z.; Gryczynski, I. Molecular fluorescence enhancement on fractal-like structures. *Appl. Spectrosc.* **2010**, *64*, 578−583.

(26) Cakmakyapan, S.; Cinel, N. A.; Cakmak, A. O.; Ozbay, E. Validation of electromagnetic field enhancement in near-infrared through Sierpinski fractal nanoantennas. *Opt. Express* **2014**, *22*, 19504−19512.

(27) Kazerooni, H.; Khavasi, A. Plasmonic fractals: ultrabroadband light trapping in thin film solar cells by a Sierpinski nanocarpet. *Opt. Quantum Electron.* **2014**, *46*, 751−757.

(28) Gottheim, S.; Zhang, H.; Alexander, O. G.; Halas, N. J. Fractal Nanoparticle Plasmonics: The Cayley Tree. *ACS Nano* **2015**, *9*, 3284−3292.

(29) Feng, J.; Siu, V. S.; Roelke, A.; Mehta, V.; Rhieu, S. Y.; Palmore, G. T. R.; Pacifici, D. Nanoscale Plasmonic Interferometers for Multispectral, High-Throughput Biochemical Sensing. *Nano Lett.* **2012**, *12*, 602−609.

(30) Cerjan, B.; Yang, X.; Nordlander, P.; Halas, N. J. Asymmetric Aluminum Antennas for Self-Calibrating Surface-Enhanced Infrared Absorption Spectroscopy. *ACS Photonics* **2016**, *3*, 354−360.

(31) Barik, A.; Otto, L. M.; Yoo, D.; Jose, J.; Johnson, T. W.; Sang-Hyun, O. Dielectrophoresis-Enhanced Plasmonic Sensing with Gold Nanohole Arrays. *Nano Lett.* **2014**, *14*, 2006−2012.

(32) Schäfer, C.; Kerna, D. P.; Fleischer, M. Capturing molecules with plasmonic nanotips in microfluidic channels by dielectrophoresis. *Lab Chip* **2015**, *15*, 1066−1071.

(33) Hein, S. M.; Giessen, H. Tailoring Magnetic Dipole Emission with Plasmonic Split-Ring Resonators. *Phys. Rev. Lett.* **2013**, *111*, No. 026803.

(34) Aigouy, L.; Cazé, A.; Gredin, P.; Mortier, M.; Carminati, R. Mapping and Quantifying Electric and Magnetic Dipole Luminescence at the Nanoscale. *Phys. Rev. Lett.* **2014**, *113*, No. 076101.

(35) Linden, S.; Enkrich, C.; Wegener, M.; Zhou, J.; Koschny, T.; Soukoulis, C. M. Magnetic Response of Metamaterials at 100 Terahertz. *Science* **2004**, *306*, 1351.

(36) Hasan, D.; Ho, C. P.; Pitchappa, P.; Lee, C. Dipolar Resonance Enhancement and Magnetic Resonance in Cross-Coupled Bow-Tie Nanoantenna Array by Plasmonic Cavity. *ACS Photonics* **2015**, *2*, 890−898.

(37) Grefe, S. E.; Leiva, D.; Mastel, S.; Dhuey, S. D.; Cabrini, S.; Schuckc, P. J.; Abate, Y. Near-field spatial mapping of strongly interacting multiple plasmonic infrared antennas. *Phys. Chem. Chem. Phys.* **2013**, *15*, 18944−18950.

(38) Lee, B.; Park, J.; Han, G. H.; Ee, H.; Naylor, C. H.; Liu, W.; Charlie Johnson, A. T.; Agarwal, R. Fano Resonance and Spectrally Modified Photoluminescence Enhancement in Monolayer MoS2 Integrated with Plasmonic Nanoantenna Array. *Nano Lett.* **2015**, *15*, 3646−3653.

(39) Wei, D.; Renaud, B.; Sergei, K.; Pascal, R.; Roch, E. Surface plasmon resonances in silver Bowtie nanoantennas with varied bow angles. *J. Appl. Phys.* **2010**, *108*, No. 124314.

DOI: 10.1021/acsomega.6b00201
ACS Omega 2016, 1, 818−831

(40) Wu, P.; Hsu, W.; Ting Chen, W.; Huang, Y.; Liao, C.; Liu, A.; Zheludev, N. I.; Sun, G.; Ping Tsai, D. Plasmon coupling in vertical split-ring resonator metamolecules. *Sci. Rep.* **2015**, *5*, No. 9726.
(41) Dregely, D.; Neubrech, F.; Duan, H.; Vogelgesang, R.; Giessen, H. Vibrational near-field mapping of planar and buried three-dimensional plasmonic nanostructures. *Nat. Commun.* **2013**, *4*, No. 2237.
(42) Lahiri, B.; McMeekin, S. G.; De La Rue, R. M.; Johnson, N. P. Enhanced Fano resonance of organic material films deposited on arrays of asymmetric split-ring resonators (A- SRRs). *Opt. Express* **2013**, *21*, 9343−9352.
(43) Liu, Y.; Hu, W.; Lua, Z.; Li, C. M. Photografted poly(methyl methacrylate)-based high performance protein microarray for hepatitis B virus biomarker detection in human serum. *MedChemComm* **2010**, *1*, 132−135.
(44) Rodrigo, S. G.; García-Vidal, F. J.; Martín-Moreno, L. Theory of absorption-induced transparency. *Phys. Rev. B.* **2013**, *88*, No. 155126.
(45) Hutchison, J. A.; O'Carroll, D. M.; Schwartz, T.; Genet, C.; Ebbesen, T. W. Absorption-Induced Transparency. *Angew. Chem., Int. Ed.* **2011**, *50*, 2085−2089.
(46) Li, W.-D.; Ding, F.; Hu, J.; Chou, S. Y. Three-dimensional cavity nanoantenna coupled plasmonic nanodots for ultrahigh and uniform surface-enhanced Raman scattering over large area. *Opt. Express* **2011**, *19*, 3925−3936.
(47) Shafiei, F.; Monticone, F.; Le, K. Q.; Liu, X.; Hartsfield, T.; Alù, A.; Li, X. A subwavelength plasmonic metamolecule exhibiting magnetic-based optical Fano resonance. *Nat. Nanotechnol.* **2013**, *8*, 95−99.
(48) Sun, Y.; Edwards, B.; Alù, A.; Engheta, N. Experimental realization of optical lumped nanocircuits at infrared wavelengths. *Nat. Mater.* **2012**, *11*, 208−212.
(49) Adato, R.; Altug, H. In-situ ultra-sensitive infrared absorption spectroscopy of biomolecule interactions in real time with plasmonic nanoantennas. *Nat. Commun.* **2012**, *4*, No. 2154.
(50) Wu, C.; Khanikaev, A. B.; Adato, R.; Arju, N.; Yanik, A. A.; Altug, H.; Shvets, G. Fano-resonant asymmetric metamaterials for ultrasensitive spectroscopy and identification of molecular monolayers. *Nat. Mater.* **2011**, *11*, 69−75.
(51) Jakšić, O. M.; Randjelovic, D. V.; Jakšic, Z. S.; Cupic, Ž. D.; Kolar-Anic, L. Z. Plasmonic sensors in multi-analyte environment: Rate constants and transient analysis. *Chem. Eng. Res. Des.* **2014**, *92*, 91−101.
(52) Querry, M. R.; Curnutte, B.; Williams, D. Refractive Index of Water in the Infrared. *J. Opt. Soc. Am.* **1969**, *59*, 1299−1305.
(53) Liu, N.; Weiss, T.; Mesch, M.; Langguth, L.; Eigenthaler, U.; Hirscher, M.; Sönnichsen, C.; Giessen, H. Planar Metamaterial Analogue of Electromagnetically Induced Transparency for Plasmonic Sensing. *Nano Lett.* **2010**, *10*, 1103−1107.
(54) Bosman, M.; Zhang, L.; Duan, H.; Tan, S. F.; Nijhuis, C. A.; Qiu, C.; Yang, J. K. W. Encapsulated Annealing: Enhancing the Plasmon Quality Factor in Lithographically− Defined Nanostructures. *Sci. Rep.* **2014**, *4*, No. 5537.
(55) Zhang, Z.; Zhao, P.; Lin, P.; Sun, F. Thermo-optic coefficients of polymers for optical waveguide applications. *Polymer* **2006**, *47*, 4893−4896.
(56) Tokmakoff, A.; Fayer, M. D. Homogeneous vibrational dynamics and inhomogeneous broadening in glass-forming liquids: Infrared photon echo experiments from room temperature to 10 K. *J. Chem. Phys.* **1995**, *103*, 2810−2826.

DOI: 10.1021/acsomega.6b00201
ACS Omega 2016, 1, 818−831